Islamic Azad University

Journal of
Optoelectronical Nanostructures

Autumn 2022 / Vol. 7, No. 4

Research Paper

Assessment of Mixed Tin-Lead Perovskite as the Absorber Material for Fabrication of Highly Sensitive Broadband Photodetector

Kosar Jafarizadeh[1], Zahra Hosseini*[,1], Hossein Amanati Manbar[1]
[1] Faculty of Advanced Technologies, Shiraz University, Shiraz, Iran

Received: 12 Aug. 2022
Revised: 8 Sep. 2022
Accepted: 15 Sep. 2022
Published: 20 Nov. 2022

Use your device to scan and read the article online

Keywords:
Broadband; High Sensitivity; Mixed Tin-Lead Perovskite; Photodetector; Self-Powered.

Abstract The relatively large bandgaps of the methylammonium lead halide perovskites are the major obstacle to achieving broadband response in the lead-based perovskite photodetectors. Partial or total substitution of lead with tin leads to smaller bandgaps for perovskite materials. Here, we investigated the application of a mixed tin-lead perovskite material, $(FASnI_3)_{0.6}(MAPbI_3)_{0.4}$, with small bandgap of 1.24 eV as the absorber material in a perovskite photodetector. The device simulation is performed by using SCAPS simulation software. The effect of different parameters such as absorber layer quality and thickness, interface defects, doping concentration and carrier mobility on the performance of the device is studied. The simulation results clarify that the parameters optimization can result in achieving a self-powered photodetector with broad spectral response from 300 to 1050 nm wavelength, a high responsivity of 0.6 A W-1 at 930 nm, almost flat detectivity of over 1013 Jones and a wide linear dynamic range. We believe this study can provide theoretical guidance for the design of highly sensitive, broadband, mixed tin-lead perovskite photodetectors.

Citation:. Assessment of Mixed Tin-Lead Perovskite as the Absorber Material for Fabrication of Highly Sensitive Broadband Photodetector.
Journal of Optoelectronical Nanostructures. 2022; 7 (4): 29- 48
DOI: 10.30495/jopn.2022.30624.1268

***Corresponding author:** Zahra Hosseini
Address: Faculty of Advanced Technologies, Shiraz University, Shiraz, Iran.
Tell: 00987136139645 **Email:** zahrahosseini@shirazu.ac.ir

1. INTRODUCTION

Photodetectors (PDs) have been widely used for a variety of industrial and scientific applications, including optical communications, environmental monitoring, day- and night-time surveillance and chemical/biological sensing [1–3]. The high-performance commercial PDs, which are mostly based on III-V compounds or silicon (Si), normally suffer from relatively low response, high driving voltage, limited spectral response, and expensive fabrication [4,5]. Therefore, it is necessary to develop PDs based on new materials and design. In the past few years, PDs based on organic semiconductors, pocessing wide spectral response range and high sensitivity, have been developed [6,7]. Recently, extensive research on solution-processed perovskite photodetectors (PPDs) have been conducted due to the outstanding optical and electrical properties of perovskites, such as large absorption coefficient, adjustable bandgaps (E_g), low defects, high mobility, long charge carrier diffusion length, and long charge carrier lifetime [8–15]. Among them, the methylammonium lead halide ($MAPbX_3$, X is Cl, Br, I) based PPDs show excellent photoelectric detection ability [16,17]. Fang et al. reported a visible PPD which can detect the light as low as sub-picowatt per square centimeter [18]. Deng et al. fabricated a PPD based on $MAPbI_3$ microwires which shows a responsivity of 13.5 A W^{-1} [19]. A phototransistor showing responsivity around 320 A W^{-1} was developed by Li et al. [20]. Although these PPDs exhibit great characteristics such as high sensitivity, fast response speed, and long linear dynamic range (LDR), their spectral response range is limited to the ultraviolet (UV) and visible range. This behaviour is the result of the relatively large E_g (>1.55 eV) of the lead-based perovskite materials. Moreover, the toxicity of Pb makes the applications of the lead-based PPDs limited.

Integration of polymers and quantum dots into the PPD has been reported as a practical strategy to extend the spectral response range of the PPD to the near-infrared (NIR) region [21,22]. However, the reported external quantum efficiency (EQE) values in NIR region are still relatively low. A proper alternative to these strategies for the extension of the spectral response range to the NIR region is the application of Low-bandgap perovskite materials in the PPD [23]. The research show that the Eg of the perovskite materials can be reduced by the partial or complete substitution of lead by tin (Sn) [24,25]. Lead-free PPDs demonstrate broader spectral response range compared to the lead-based PPDs, but they usually have relatively low responsivity and gain. In 2016, Zhao and co-workers showed that the E_g of mixed Sn-Pb perovskite $CH_3NH_3(Pb_xSn_{1-x})I_3$ $[0 \leq x \leq 1]$ is

tunable from 1.2 to 2.4 eV by adjusting the molar ratio of Sn to Pb [26]. This implies that one can extend the absorption edge of mixed Sn-Pb perovskites to the NIR region. Therefore, the mixed Sn-Pb perovskites are suitable candidates as the absorber material for fabrication of broad-band PPDs. Nevertheless, the stability of mixed Sn-Pb perovskites are deteriorated significantly by the oxidation of Sn^{2+}. Different strategies have been reported to suppress Sn^{2+} oxidation such as partial substitution of MA cation with FA (FA = formamidinium) cation or using tin fluoride (SnF_2) additives [27,28]. In spite of the great potential of low-bandgap tin-lead perovskites in obtaining sensitive broadband PPDs, the experimental reports on the application of low bandgap tin-lead perovskites in the PPDs are rare. In 2017, Xu et al. reported low-bandgap $MA_{0.5}FA_{0.5}Pb_{0.5}Sn_{0.5}I_3$ based PPDs with broadband response range from UV to the NIR [29]. In the same year, Wang et al. demonstrated highly sensitive PPD based on tin-lead, exhibiting a broadband response from 300-1000 nm [30]. Zhao et al. demonstrated a Sn-Pb PPD with double sided passivation structure which contribute an EQE close to 80% from 300 to 1050 nm [23]. Moreover, the investigation of the materials and the device properties, and the relationship between the structure parameters and the PD performance in a mixed tin-lead PPD are rather scarce. Device simulation clarifies the relationship between the materials properties and the device performance. To the best of our knowledge, there has been no report on simulation of PPDs based on tin-lead perovskite materials. In this paper, we report on the simulation of a $(FASnI_3)_{0.6}(MAPbI_3)_{0.4}$ PPD using 1D-solar cell capacitance simulator (SCAPS, ver.3.3.09). We investigated the effects of different parameters, such as the absorber thickness, the defect density in the absorber, the interface defect density, doping condition and carrier mobilities on the performance of the PPD. Giving a deep insight, we believe the simulation results in this paper will give a beneficial guideline for designing highly sensitive self-powered broadband PPDs.

2. 2. DEVICE SIMULATION PARAMETERS

One dimensional SCAPS-1D device simulation software version 3.3.09, developed by Department of Electronics and Information systems (ELIS) of University of Gent of Belgium, was utilized [31]. The inverted structure of the $(FASnI_3)_{0.6}(MAPbI_3)_{0.4}$ PPD investigated here is composed of ITO/hole transport material (HTM)/$(FASnI_3)_{0.6}(MAPbI_3)_{0.4}$/electron transport material (ETM)/Ag [32]. $(FASnI_3)_{0.6}(MAPbI_3)_{0.4}$ is the absorber material, and the PPD has P-type poly(3,4-ethylenedioxythiophene) polystyrene sulfonate (PEDOT: PSS) as organic HTM and n-type fullerene (C_{60}) as organic ETM.

The various physical properties of the materials used in this work have been described in Table I. Table II shows the detailed information on the physical

properties of interfaces and defect density. The values reported in Table I and Table II are used for the simulation in this work. The electron surface recombination velocity is kept at 10^5 cm s^{-1} for the back end and 10^7 cm s^{-1} for the front end. The E_g of perovskite active material is 1.24 eV [32]. In the simulation, pre-factor A_α is assumed to be 1×10^5 to obtain absorption coefficient (α) curve calculated by $\alpha^{¼}A_\alpha(h\upsilon\text{-}E_g)^{1/2}$, where the $h\upsilon$ is the photon energy [33]. The optical reflectance at the surface and interfaces of each layer is ignored in this simulation. A series resistance is assumed to be 2.7 Ω cm^2. E_t in Table II is located at the center of E_g and distributed in Gaussian with characteristic energy of 0.1 eV, where the defect type is neutral. All the simulations are performed under AM1.5G (100 mW cm^{-2}) illumination unless clearly quoted.

To validate the simulation parameters taken in our study, we have firstly regenerated the experimental results published by Chongwen Li et al., in which a solar cell with a similar structure to the structure in this report is fabricated [32]. Figure. S1 in supplementary material (SI), shows the experimental J-V characteristics of the $(FASnI_3)_{0.6}(MAPbI_3)_{0.4}$ perovskite solar cell in [32], together with the simulated data. The simulated results show a close match to the experimental results which confirms the validation of the parameters used in the simulation.

Table 1: Properties of HTM, absorber and ETM, used in the simulation of the PPD.

	PEDOT: PSS	$(FASnI_3)_{0.6}(MAPbI_3)_{0.4}$	C_{60}
Thickness (nm)	30[30]	620[32]	20[32]
E_g (eV)	1.6 [34]	1.24[32]	1.9 [35]
Electron affinity (X_a) (eV)	3.6[36]	4.15 [37]	4.2 [38]
Relative permittivity	3 [34]	4 [33]	4.2 [38]
Effective conduction band density (N_c) (cm^{-3})	1×10^{22} [34]	1×10^{19} [39]	1×10^{20} [38]
Effective valance band density (N_v) (cm^{-3})	1×10^{22}[34]	2×10^{18}[39]	1×10^{20} [38]
Electron mobility (μ_n) (cm^2 V^{-1} s^{-1})	4.5×10^{-4}[34]	1[32]	0.01 [38]
Hole mobility (μ_p) (cm^2 V^{-1} s^{-1})	9.9×10^{-5} [34]	3.5[32]	0.01 [38]
Donor concentration (N_D) (cm^{-3})	–	–	2.6×10^{18} [40]
Acceptor concentration (N_A) (cm^{-3})	2×10^{18} [34]	4.7×10^{15} [32]	–

Table 2: The information on the physical properties of interfaces and defect densities used in the simulation.

	PEDOT: PSS	$(FASnI_3)_{0.6}(MAPbI_3)_{0.4}$	C_{60}[41]	HTM/ Absorber	Absorber /ETM
defect type	Neutral	Neutral	Single Acceptor	Neutral	Neutral
capture cross section for electrons (cm^2)	1×10^{-15}	1×10^{-15}	1×10^{-15}	1×10^{-19}	1×10^{-19}
capture cross section for holes (cm^2)	1×10^{-15}	1×10^{-15}	1×10^{-15}	1×10^{-19}	1×10^{-19}
energetic distribution	Single	Single	Gaussian	Single	Single
reference for defect energy level (E_t)	above E_V	above E_V	above E_V	above E_V	above E_V
energy level with respect to Reference (eV)	0.6	0.6	0.6	0.6	0.6
Defect density (N_t) (cm^{-3})	1×10^{14}[42]	3×10^{14} [43]	1×10^{14}	5.5×10^{9}	1×10^{10}

3. RESULTS AND DISCUSSION

A. Effect of Carrier Diffusion Length and Absorber Thickness

In a PPD, photo-generated charge carriers are created in the perovskite absorber. Diffusion process takes place in the bulk region of the absorber due to the concentration gradient. Then, on both sides of the absorber, at HTM/absorber and absorber/ETM interfaces, the charge carriers are separated and move in different directions under electric field. Therefore, both the absorber quality, i.e., carrier diffusion length for electron (L_n) and hole (L_p), and absorber layer thickness are limiting parameters for the PD performance.

Carrier diffusion length is defined as [44]

$$L = \sqrt{D \times \tau} \quad (1)$$

D and τ are diffusion coefficient and carrier life time and are represented by equations 2 and 3, respectively.

$$D = \frac{\mu K_B T}{q} \quad (2)$$

$$\tau_{np} = \frac{1}{\sigma_{np}.\vartheta_{th}.N_t} \quad (3)$$

where T is the *temperature* in Kelvin, K_B is the Boltzmann constant, and q represents the magnitude of charge. ϑ_{th} and $\sigma_{n,p}$ denote the thermal velocity and

capture cross section of electron and hole, whereas N_t represents the defect density.

The equations 1-3 show that in a constant temperature, the diffusion length of electrons and holes are affected by the defect density in the absorber layer. Figure. 1a shows the short circuit current density (J_{sc}) as a function of L_n in the absorber layer. L_n was changed from 0.16 to 16 μm by changing N_t from 1×10^{16} to 1×10^{12} (cm^{-3}). The strong impact of the L_n on J_{sc} is observed when L_n is less than 2 μm which is corresponding to the defect densities greater than 1×10^{14} (cm^{-3}) in the absorber layer. For L_n greater than 2 μm, J_{sc} is almost unaffected by L_n and saturates to 31 mA/cm^2. The device simulation indicates that the experimentally reported value of $L_n \sim 1$ μm [45] is not long enough to guarantee an excellent carrier collection. Decreasing the defect density in the absorber layer leads to an increase in the L_n and thereby better carrier collection in the absorber layer. Moreover, if the carrier collection is excellent, the increase of the absorber thickness for the complete absorption of incident illumination will be beneficial for further improvement of the PPD performance. It is worth mentioning that since the PPD has inverted structure in this study, and the L_p is usually large enough, the L_p is not considered as a limiting parameter on the performance of the $(FASnI_3)_{0.6}(MAPbI_3)_{0.4}$ PPD. The corresponding L_ps for different defect densities in the absorber layer are reported in the inset of Figure. 1a.

Figure. 1b shows the variation of J_{sc} with the absorber thickness for different electron diffusion lengths in the $(FASnI_3)_{0.6}(MAPbI_3)_{0.4}$ perovskite. Here, the absorber thickness was varied from 100 nm to 1000 nm. When a thin absorber layer of 100 nm is used, the photo-generated current density is as low as 21 mA/cm^2 for all electron diffusion lengths. When the absorber quality is high ($L_n > 1.6$ μm), J_{sc} increases with increasing the absorber layer thickness, and reaches a saturation at value of around 31.2 mA/cm^2. This can be attributed to the much photon absorption and thereby much carrier generation in a thicker absorber layer. If the quality of the absorber layer is not good enough ($L_n < 1.6$ μm), the recombination in the absorber layer becomes dominant as shown in Figure. 1c and the reciprocal relation between photon absorption and carrier collection in the absorber layer is much obvious. The J_{sc} first increases and then decreases by increasing the absorber thickness when L_n is smaller than 1.6 μm (Figure. 1b). Hence, the optimum thickness of the absorber layer for generating the highest amount of J_{sc} is different for different absorber layer qualities, i.e., different L_n. Figure. 1d. shows the variation of the optimum thickness of the absorber layer with the L_n in the absorber layer. When L_n is around 1.6 μm, the optimum thickness of the absorber layer for attaining the maximum achievable J_{sc} is around

500 nm, while the value of the optimum thickness reduces to around 400 nm and 300 nm when L_n is 500 nm and 160 nm, respectively. The simulation results show that the desirable thickness is determined by both the absorption efficiency and the absorber quality. If the carrier collection is excellent (large L_n), the increase of the absorber thickness for the complete absorption of incident illumination will be beneficial for further improvement of the current density and thereby the responsivity of the PPD.

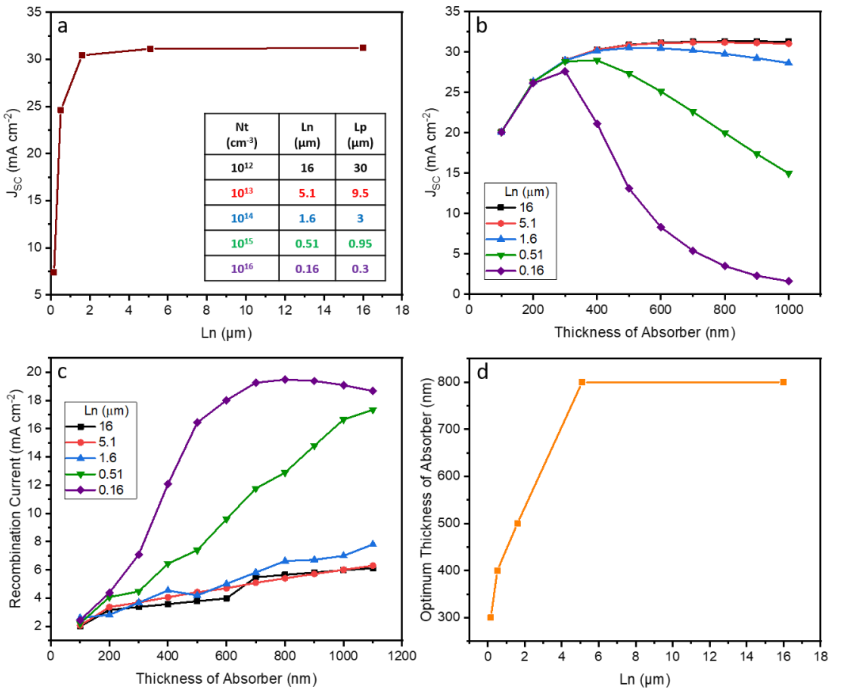

Fig. 1. (a) J_{sc} as a function of L_n in the absorber layer. (b) Variation of J_{sc} with the absorber thickness, and (c) recombination current vs thickness of the absorber, for different L_n in the $(FASnI_3)_{0.6}(MAPbI_3)_{0.4}$ perovskite. (d) variation of the optimum thickness of the absorber layer with the L_n in the absorber layer.

In order to clarify how the absorber layer thickness affect the responsivity and response range of the $(FASnI_3)_{0.6}(MAPbI_3)_{0.4}$ PPD, the plots of responsivity vs wavelength for the PPDs with absorber layers of different thicknesses are demonstrated in Figure. 2. The data reported in Figure. 2 are generated for an absorber layer with $L_n \sim 1$ μm. It is clear that the responsivity of the

$(FASnI_3)_{0.6}(MAPbI_3)_{0.4}$ PPD can be noticeably improved with the increase of the absorber layer thickness, especially in the long wavelength range. Nevertheless, increasing the absorber thickness over an optimum value of around 500 nm, leads to a decrease in the responsivity, especially in short wavelength range. This can be attributed to the higher recombination rate in thick absorber layers. These results imply that a relatively thick $(FASnI_3)_{0.6}(MAPbI_3)_{0.4}$ perovskite layer, as the absorber layer, in the PPD is needed in order to have a large responsivity in a broad wavelength range including the NIR region.

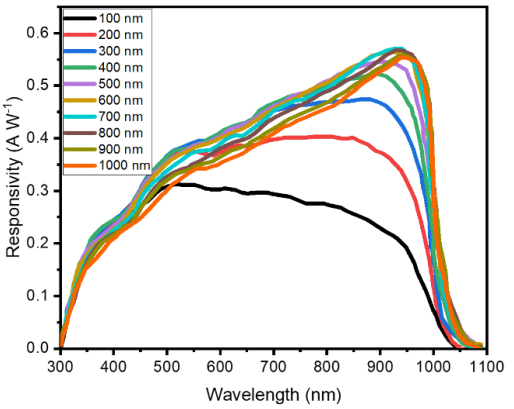

Fig. 2. Responsivity vs wavelength for the $(FASnI_3)_{0.6}(MAPbI_3)_{0.4}$ PPDs with absorber layers of different thicknesses.

B. Effect of Interface Defect

The interface quality is another parameter affecting the performance of the $(FASnI_3)_{0.6}(MAPbI_3)_{0.4}$ PPD. The photo-generated charge carriers meet the defects and thereby recombine at the HTM/absorber interface or absorber/ETM interface on their way to the charge collectors in the device. Zhao et al. reported the presence of different kinds of defects such as defects of iodide anions at the interfaces of a tin-lead perovskite device [23]. They also stated that the massive PbI_2 surplus at the interface between the bottom perovskite layer and the hole transport layer, had negative effects on crystal growth of the tin-lead perovskite and can easily lead to more defects [23]. Here, we investigated the $(FASnI_3)_{0.6}(MAPbI_3)_{0.4}$ PPD performance by changing the defect densities at the interfaces to reveal the trend of the significance of the interface quality. The defect densities of the HTM/absorber and the absorber/ETM interfaces were changed

from 1×10^{7} to 1×10^{13} cm^{-3}. Figure. 3a shows the J_{sc} variation by defect densities at the HTM/absorber and absorber/ETM interfaces for the $(FASnI_3)_{0.6}(MAPbI_3)_{0.4}$ PPD. Figure. 3a indicates that the defect density at the HTM/absorber interface has a strong impact on the J_{sc} when the value of the defect density is more than 10^{10} cm^{-3}. On the other hand, the J_{sc} variation by the defect density at the absorber/ETM interface is negligible. These results imply that the interface quality at the HTM/absorber interface has more significant impact on the $(FASnI_3)_{0.6}(MAPbI_3)_{0.4}$ PPD performance than that at the absorber/ETM interface. This difference can be attributed to the inverted structure of the PPD. In a PPD with inverted structure, the illumination takes place from the HTM/absorber interface side. Since the absorption coefficient of the $(FASnI_3)_{0.6}(MAPbI_3)_{0.4}$ absorber layer is high, the incident light is mostly absorbed near the HTM/absorber interface. Therefore, as it is shown in Figure. 3b, the generation rate of electron-hole pairs at HTM/absorber interface is much higher than the generation rate at the absorber/ETM interface. This implies that more counter carriers are available for recombination at the HTM/absorber interface defects compared to the absorber/ETM interface. Therefore, as it is demonstrated in Figure. 3c, variation of the defect density at the HTM/absorber interface has a more pronounced effect on the recombination current compared to the absorber/ETM interface. Figure. 3c shows the recombination current in the device at different interface defect densities for both HTM/absorber and absorber/ETM interfaces. For all interface defect densities, the recombination current caused by the defects at the HTM/absorber interface is much higher than the recombination current caused by the defects at the absorber/ETM interface. Moreover, the recombination current in the device increases drastically by the increase in HTM/absorber interface defect density in the range of 10^{9}-10^{13} cm^{-3}, while a similar change in the absorber/ETM interface defect density does not change the recombination current significantly. The simulation results in this part show that the improvement of the interface quality, especially the HTM/absorber interface, leads to a high responsivity of over 0.55 A W^{-1} in the NIR region for the $(FASnI_3)_{0.6}(MAPbI_3)_{0.4}$ PPD. The plots of EQE, responsivity and detectivity of the $(FASnI_3)_{0.6}(MAPbI_3)_{0.4}$ PPD for different HTM/absorber interface defect densities are provided in Figure. S2.

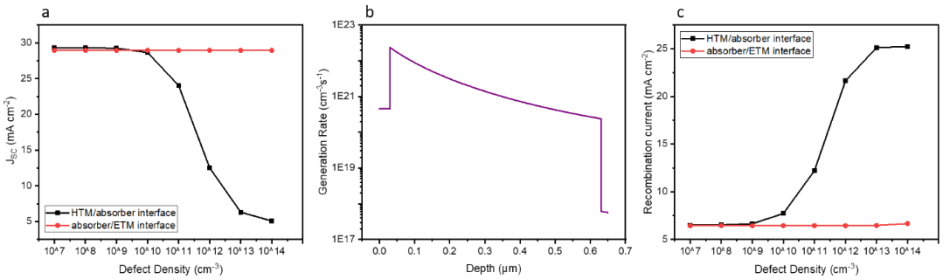

Fig. 2. (a) The J_{sc} variation by the defect densities at the HTM/absorber and absorber/ETM interfaces for the $(FASnI_3)_{0.6}(MAPbI_3)_{0.4}$ PPD. (b) carrier generation rate profile in the $(FASnI_3)_{0.6}(MAPbI_3)_{0.4}$ PPD. (c) The recombination current in the $(FASnI_3)_{0.6}(MAPbI_3)_{0.4}$ PPD as a function of interface defect densities.

C. Effect of Doping Condition of the Absorber Layer

Easy oxidation of Sn^{2+} to Sn^{4+} in the perovskites containing tin, facilitates the formation of tin vacancies in the perovskite material and acts as an acceptor dopant within the material [43]. Therefore, in the simulation of PPD based on $(FASnI_3)_{0.6}(MAPbI_3)_{0.4}$ perovskite, we considered an acceptor density (N_A) in the range of 10^{13} to 10^{18} cm^{-3} inside the absorber layer. The results for the effect of N_A on the J_{sc} of the $(FASnI_3)_{0.6}(MAPbI_3)_{0.4}$ PPD is shown in Figure. 4a. J_{sc} is almost constant when N_A is small and decreases rapidly when N_A exceeds 10^{15} cm^{-3}. The energy band diagrams and recombination rates of PPDs for different N_A in the absorber are presented in Figure. 4b and Figure. 4c, respectively. When N_A is higher than 10^{15} cm^{-3}, the recombination rates both near the HTM/absorber interface and in the bulk are enhanced (Figure. 4c). Therefore, increased acceptor density in the absorber layer causes the suppression of hole and electron transfer from absorber to the HTM and the ETM layers, leading to a decrease in J_{sc}. Thus, the doping density is markedly effective on the properties of $(FASnI_3)_{0.6}(MAPbI_3)_{0.4}$ PPD. Different strategies have been suggested in the literature in order to decrease the oxidation of Sn^{2+} in tin-lead perovskites. Partial substitution of MA cation with FA cation or using SnF_2 additives has been reported to suppress Sn^{2+} oxidation in the mixed Sn-Pb perovskites [30]. Adding Bromide (Br) to $(FASnI_3)_{0.6}(MAPbI_3)_{0.4}$ compound will also reduce hole density, thus reducing Sn^{2+}oxidation [32]. SnF_2 derivative coordinated with DMSO molecules such as a $[SnF_2(DMSO)]_2$ complex can also suppress the Sn^{2+} oxidation [46].

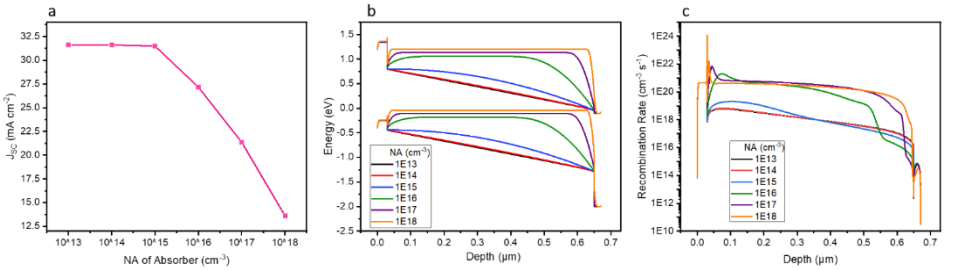

Figure 3. (a) Variation of J_{sc} as a function of N_A in the $(FASnI_3)_{0.6}(MAPbI_3)_{0.4}$ perovskite layer. The (b) energy band diagrams, and (c) recombination rates of $(FASnI_3)_{0.6}(MAPbI_3)_{0.4}$ PPDs for different N_A in the absorber

D. Effect of Carrier Mobilities in the Absorber Layer

The high responsivity of a PPD is resulted from different characteristics of the absorber layer such as direct band gap with high absorption coefficient, long carrier diffusion lengths as well as large and balanced electron and hole mobilities. Therefore, investigating the impact of carrier mobility on the PPD performance will be of great significance. In this section we demonstrate how carrier mobility, as a basic parameter, plays role in light detection by a $(FASnI_3)_{0.6}(MAPbI_3)_{0.4}$ PPD. Figure. 5a gives the J_{sc} curves as a function of the electron and hole mobilities in $(FASnI_3)_{0.6}(MAPbI_3)_{0.4}$ perovskite. A large carrier mobility is definitely beneficial to the high current generation and thereby high responsivity of the PPD, but as it is demonstrated in Figure 5a, J_{sc} increases with the increase in electron mobility while it stays almost unchanged with the increase in the hole mobility. The difference in the trends of J_{sc} variation by electron and hole mobilities arises from the different path lengths for the electrons and holes in the absorber layer. As explained before, in an inverted structure, the incident light absorption and thereby the electron-hole pair generation mainly happens near the HTM/absorber interface (Figure. 3b). This implies that the electrons need to pass a longer path inside the absorber layer compared to the holes path before they reach the corresponding transport layers. When electron mobility increases, the recombination of the photo-generated carriers reduces considerably. This behavior is more obvious in the bulk of the perovskite layer and near the HTM/absorber interface and is demonstrated in the Figure. 5b which shows the recombination rate in the $(FASnI_3)_{0.6}(MAPbI_3)_{0.4}$ PPD for different electron mobilities. Electron mobility has a remarkable effect on the recombination rate in the perovskite layer while hole mobility does not change the recombination rate in the bulk of the absorber layer significantly. However, Figure. 5c shows that the

recombination rate near the absorber/ETM interface reduces by increasing the hole mobility in the absorber layer. Electrons with low mobility are difficult to transport in the perovskite layer and reach the ETM. They accumulate in the absorber layer and recombine with other carriers. Therefore, the electron mobility has a more significant effect on the current generation in the $(FASnI_3)_{0.6}(MAPbI_3)_{0.4}$ PPD compared to the hole mobility.

Moreover, higher carrier mobility results in larger diffusion length (see equations 2 & 3). According to the discussions in section effect of interface deffect, thicker absorber layers can be used in the PPD when the diffusion lengths are larger. Therefore, higher carrier mobility will let us to make PPDs with thicker $(FASnI_3)_{0.6}(MAPbI_3)_{0.4}$ perovskite layer and thereby have PPDs with broader response range. One can say that for having a broadband PPD with high EQE and responsivity in NIR region, high electron mobility inside the $(FASnI_3)_{0.6}(MAPbI_3)_{0.4}$ layer is essential.

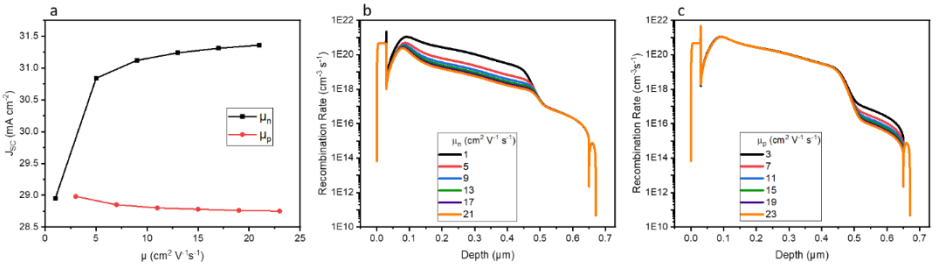

Fig. 4. (a) J_{sc} curve as a function of the electron and hole mobilities in $(FASnI_3)_{0.6}(MAPbI_3)_{0.4}$ perovskite. The recombination rate in the $(FASnI_3)_{0.6}(MAPbI_3)_{0.4}$ PPD for different (b) electron mobilities, and (c) hole mobilities.

E. The Performance of the Optimum $(FASnI_3)_{0.6}(MAPbI_3)_{0.4}$ PPD

In this section, a mixed tin-lead PPD based on the optimum parameters discussed in the previous sections is simulated. Figure. 6a shows the simulated J–V curve of the self-powered PPD both in dark and under the illumination of AM 1.5G solar spectrum. The device shows a very low short circuit dark current (of the order of nA/cm^2) while the short circuit current density under light illumination reaches a value as high as 32 mA/cm^2. This ensures a high photosensitivity for the mixed tin-lead PPD [47]. The corresponding EQE, responsivity and detectivity of the simulated PPD are provided in Figure. 6b-6d. These parameters are the most important parameters for evaluating the efficiency of the PPD. Responsivity is severely linked to the EQE, which demonstrates the ability of the PPD to convert the incident photons into current in varied wavelengths. Both Figure 6b and 6c

show a broad spectral response range from UV to NIR for the $(FASnI_3)_{0.6}(MAPbI_3)_{0.4}$ PPD. The overall EQE is more than 80% and maintains average values in the NIR region. The high EQE in the NIR region can help the PPD to have higher responsivity in this part. The responsivity in the wavelengths between 750 nm and 990 nm is over 0.5 A W^{-1} and it reaches 0.6 A W^{-1} at 930 nm. These results imply that the responsivity of a broadband mixed tin-lead PPD can be considerably higher than that of the conventional Si-based photodiodes. The calculated detectivity of the PPD, which demonstrated the ability of devices in detecting low intensity light, is plotted in Figure 6d. As can be seen, the optimized $(FASnI_3)_{0.6}(MAPbI_3)_{0.4}$ PPD exhibits almost flat detectivity of over 10^{13} Jones in a broad spectral range from 350 to 1000 nm, suggesting the high performance of the simulated mixed tin-lead PPD. Notably, it is of great importance that this PPD can provide a detectivity in NIR region as high as the detectivity in visible spectrum.

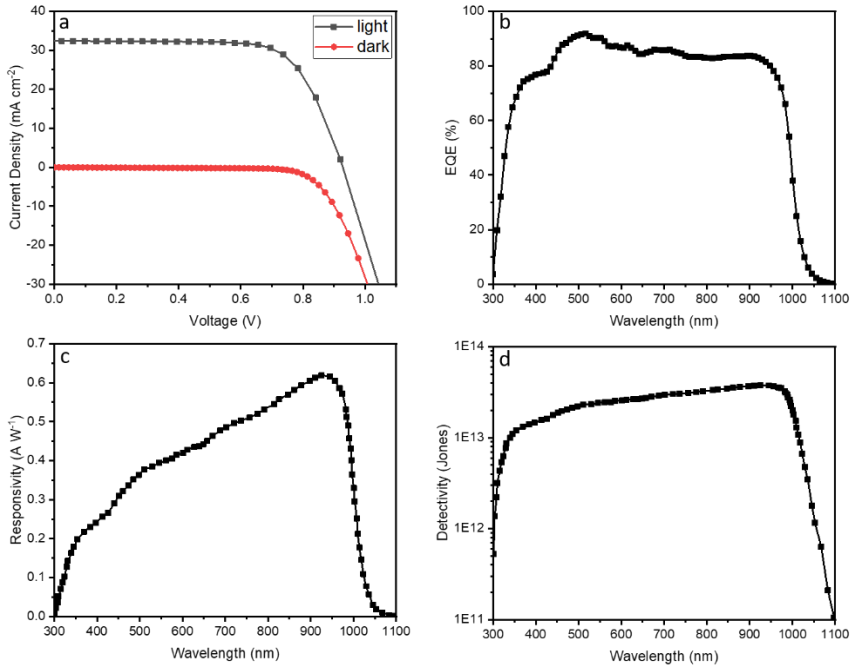

Figure 5. (a) J–V curves of the optimized $(FASnI_3)_{0.6}(MAPbI_3)_{0.4}$ PPD simulated in dark and under AM 1.5G illumination. (b) EQE spectrum, (c) responsivity, and (D) detectivity of the optimized $(FASnI_3)_{0.6}(MAPbI_3)_{0.4}$ PPD.

Another important figure of merit for a PPD is its LDR, which exhibits a region where the PPD current changes linearly with the incident light intensity.

Therefore, the light signal intensity can be precisely detected in this range. The simulated LDR for the $(FASnI_3)_{0.6}(MAPbI_3)_{0.4}$ PPD is calculated under varied light intensities of monochromatic light of 930 nm as shown in figure 7. Intriguingly, the optimized $(FASnI_3)_{0.6}(MAPbI_3)_{0.4}$ PPD shows a wide LDR extended to 10^{-8} W m^{-2}, suggesting that the PPD has the capability to detect light with a large light intensity range.

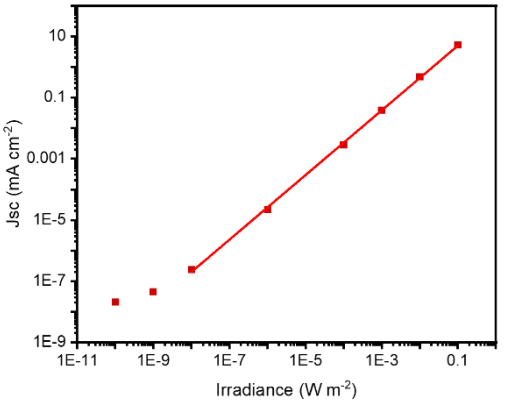

Figure 6. The linear dynamic range (LDR) of the optimized $(FASnI_3)_{0.6}(MAPbI_3)_{0.4}$ PPD.

4. CONCLUSION

In this study, we demonstrated the high potential of the mixed tin-lead perovskite material as the absorber material in a broadband PD. A device simulation of PPD with the structure of ITO/PEDOT:PSS/$(FASnI_3)_{0.6}(MAPbI_3)_{0.4}$/$C_{60}$/Ag has been done showing the impact of different parameters on the device performance. The simulation approach is based on the individual variation of device parameters to see its impact on the PPD performance and to gain a deep insight on the reason behind its influence. Simulation results show that the optimum thickness of the absorber layer is highly affected by the quality of this layer. In the case of high absorber layer quality (L_n > 1.6 µm), absorber layers thicker than 500 nm can be used in the $(FASnI_3)_{0.6}(MAPbI_3)_{0.4}$ PPD in order to satisfy the full absorption of the incident light. We investigated the effect of the interface defects and realized that a high defect density at the HTM/absorber interface cause a more intense recombination rate in the $(FASnI_3)_{0.6}(MAPbI_3)_{0.4}$ PPD with inverted structure compared to the defects at the absorber/ETM interface. Another main issue in these PPDs is the doping concentration (N_A). Our results show that

$(FASnI_3)_{0.6}(MAPbI_3)_{0.4}$ PPDs with lower N_A have better performance. Therefore, the proper strategies need to be hired in the fabrication of the devices to suppress the formation of Sn^{4+} in the absorber layer. In addition, our simulation results show that the carrier mobilities in $(FASnI_3)_{0.6}(MAPbI_3)_{0.4}$ perovskite layer is large enough to provide a high J_{sc} in the PPD. When including all parameters optimization, the final $(FASnI_3)_{0.6}(MAPbI_3)_{0.4}$ PPD show a self-powered response in a broad spectral range from 300 to 1050 nm, a high responsivity of 0.6 A W^{-1} at 930 nm, almost flat detectivity of over 10^{13} Jones and a wide LDR. The optimized $(FASnI_3)_{0.6}(MAPbI_3)_{0.4}$ PPD show much higher responsivity and detectivity compared to the experimental results reported for the mixed tin-lead PPDs [23,29,30], implying the higher potential of the mixed tin-lead perovskites as the absorber material in PPD. We believe that these results can provide important guidelines for designing self-powered, highly sensitive, broadband, mixed tin-lead PPDs which is desirable for practical applications.

CONFLICT OF INTEREST

The authors state that publication of this manuscript does not involve any conflicts of interest.

REFERENCES

[1] L. Dou, Y.M. Yang, J. You, Z. Hong, W.H. Chang, G. Li, Y. Yang, *Solution-processed hybrid perovskite photodetectors with high detectivity*, Nat. Commun. 5 (2014) 1–6. doi:10.1038/ncomms6404.

[2] H.R.S. Saman Salimpour, *Impressive Reduction of Dark Current in InSb Infrared Photodetector to achieve High Temperature Performance*, J. Optoelectron. Nanostructures. 3 (2018) 81–96. doi:20.1001.1.24237361.2018.3.4.7.4.

[3] H.G.-B.-O. Somaye Jalaei, Javad Karamdel, *Black Phosphorus Mid-Infrared Photodetector with Circular Au/Pd Antennas*, J. Optoelectron. Nanostructures. 7 (2022) 37–54. doi:10.30495/JOPN.2022.29104.1239.

[4] X. Qiu, X. Yu, S. Yuan, Y. Gao, X. Liu, Y. Xu, D. Yang, *Trap Assisted Bulk Silicon Photodetector with High Photoconductive Gain, Low Noise, and Fast Response by Ag Hyperdoping*, Adv. Opt. Mater. 6 (2018) 1–8. doi:10.1002/adom.201700638.

[5] I. Vurgaftman, J.R. Meyer, L.R. Ram-Mohan, *Band parameters for III-V compound semiconductors and their alloys*, J. Appl. Phys. 89 (2001) 5815–5875. doi:10.1063/1.1368156.

[6] C. Liu, K. Wang, C. Yi, X. Shi, P. Du, A.W. Smith, A. Karim, X. Gong, *Ultrasensitive solution-processed perovskite hybrid photodetectors*, J. Mater. Chem. C. 3 (2015) 6600–6606. doi:10.1039/c5tc00673b.

[7] K. Wang, C. Liu, C. Yi, L. Chen, J. Zhu, R.A. Weiss, X. Gong, *Efficient Perovskite Hybrid Solar Cells via Ionomer Interfacial Engineering*, Adv. Funct. Mater. 25 (2015) 6875–6884. doi:10.1002/adfm.201503160.

[8] H.-S. Rao, W.-G. Li, B.-X. Chen, D.-B. Kuang, C.-Y. Su, I*n Situ Growth of 120 cm^2 $CH_3NH_3PbBr_3$ Perovskite Crystal Film on FTO Glass for Narrowband-Photodetectors*, Adv. Mater. 29 (2017) 1602639. doi:10.1002/adma.201602639.

[9] M.M. Lee, J. Teuscher, T. Miyasaka, T.N. Murakami, H.J. Snaith, *Efficient Hybrid Solar Cells Based on Meso-Superstructured Organometal Halide Perovskites*, Science. 338 (2012) 643–647. doi:10.1126/science.1228604.

[10] Y. Fang, Q. Dong, Y. Shao, Y. Yuan, J. Huang, *Highly narrowband perovskite single-crystal photodetectors enabled by surface-charge recombination*, Nat. Photonics. 9 (2015) 679–686. doi:10.1038/nphoton.2015.156.

[11] R. Liu, J. Zhang, H. Zhou, Z. Song, Z. Song, C.R. Grice, D. Wu, L. Shen, H. Wang, *Solution-Processed High-Quality Cesium Lead Bromine Perovskite Photodetectors with High Detectivity for Application in Visible Light Communication*, Adv. Opt. Mater. 8 (2020) 1–7. doi:10.1002/adom.201901735.

[12] H. Zhou, Z. Song, C.R. Grice, C. Chen, J. Zhang, Y. Zhu, R. Liu, H. Wang, Y. Yan, *Self-powered $CsPbBr_3$ nanowire photodetector with a vertical structure*, Nano Energy. 53 (2018) 880–886. doi:10.1016/j.nanoen.2018.09.040.

[13] M.M.A. Shahram Rafiee Rafat, Zahra Ahangari, *Performance Investigation of a Perovskite Solar Cell with TiO2 and One Dimensional ZnO Nanorods as Electron Transport Layers*, J. Optoelectron. Nanostructures. 6 (2021) 75–90. doi: 10.30495/JOPN.2021.28208.1224.

[14] A.N. Seyyed Reza Hosseini, Mahsa Bahramgour, Nagihan Delibas, *A Simulation Study around Investigating the Effect of Polymers on the Structure and Performance of a Perovskite Solar Celle*, J. Optoelectron. Nanostructures. 7 (2022) 37–50. doi:10.30495/JOPN.2022.29720.1252.

[15] A.K.S. Davood Jalalian, Abbas Ghadimi, *Investigation of the Effect of Band Offset and Mobility of Organic/Inorganic HTM Layers on the Performance*

of Perovskite Solar Cells, J. Optoelectron. Nanostructures. 5 (2020) 65–78. doi: 20.1001.1.24237361.2020.5.2.6.3.

[16] D. Wu, H. Zhou, Z. Song, M. Zheng, R. Liu, X. Pan, H. Wan, J. Zhang, H. Wang, X. Li, H. Zeng, *Welding Perovskite Nanowires for Stable, Sensitive, Flexible Photodetectors*, ACS Nano. 14 (2020) 2777–2787. doi:10.1021/acsnano.9b09315.

[17] Z. Cheng, K. Liu, J. Yang, X. Chen, X. Xie, B. Li, Z. Zhang, L. Liu, C. Shan, D. Shen, *High-Performance Planar-Type Ultraviolet Photodetector Based on High-Quality $CH_3NH_3PbCl_3$ Perovskite Single Crystals*, ACS Appl. Mater. Interfaces. 11 (2019) 34144–34150. doi:10.1021/acsami.9b09035.

[18] Y. Fang, J. Huang, *Resolving weak light of sub-picowatt per square centimeter by hybrid perovskite photodetectors enabled by noise reduction*, Adv. Mater. 27 (2015) 2804–2810. doi:10.1002/adma.201500099.

[19] W. Deng, X. Zhang, L. Huang, X. Xu, L. Wang, J. Wang, Q. Shang, S.T. Lee, J. Jie, *Aligned Single-Crystalline Perovskite Microwire Arrays for High-Performance Flexible Image Sensors with Long-Term Stability*, Adv. Mater. 28 (2016) 2201–2208. doi:10.1002/adma.201505126.

[20] F. Li, C. Ma, H. Wang, W. Hu, W. Yu, A.D. Sheikh, T. Wu, *Ambipolar solution-processed hybrid perovskite phototransistors*, Nat. Commun. 6 (2015) 1–8. doi:10.1038/ncomms9238.

[21] C. Liu, K. Wang, P. Du, E. Wang, X. Gong, A.J. Heeger, *Ultrasensitive solution-processed broad-band photodetectors using $CH_3NH_3PbI_3$ perovskite hybrids and PbS quantum dots as light harvesters*, Nanoscale. 7 (2015) 16460–16469. doi:10.1039/c5nr04575d.

[22] Y. Wang, D. Yang, X. Zhou, D. Ma, A. Vadim, T. Ahamad, S.M. Alshehri, *Perovskite/Polymer Hybrid Thin Films for High External Quantum Efficiency Photodetectors with Wide Spectral Response from Visible to Near-Infrared Wavelengths*, Adv. Opt. Mater. 5 (2017) 1–6. doi:10.1002/adom.201700213.

[23] Y. Zhao, C. Li, J. Jiang, B. Wang, L. Shen, *Sensitive and Stable Tin–Lead Hybrid Perovskite Photodetectors Enabled by Double-Sided Surface Passivation for Infrared Upconversion Detection*, Small. 16 (2020) 2001534. doi:10.1002/smll.202001534.

[24] J. Im, C.C. Stoumpos, H. Jin, A.J. Freeman, M.G. Kanatzidis, *Antagonism between Spin-Orbit Coupling and Steric Effects Causes Anomalous Band Gap Evolution in the Perovskite Photovoltaic Materials $CH_3NH_3Sn_{1-x}Pb_xI_3$*,

J. Phys. Chem. Lett. 6 (2015) 3503–3509. doi:10.1021/acs.jpclett.5b01738.

[25] T. Nakamura, S. Yakumaru, M.A. Truong, K. Kim, J. Liu, S. Hu, K. Otsuka, R. Hashimoto, R. Murdey, T. Sasamori, H. Do Kim, H. Ohkita, T. Handa, Y. Kanemitsu, A. Wakamiya, *Sn(IV)-free tin perovskite films realized by in situ Sn(0) nanoparticle treatment of the precursor solution*, Nat. Commun. 11 (2020) 3008. doi:10.1038/s41467-020-16726-3.

[26] B. Zhao, M. Abdi-Jalebi, M. Tabachnyk, H. Glass, V.S. Kamboj, W. Nie, A.J. Pearson, Y. Puttisong, K.C. Gödel, H.E. Beere, D.A. Ritchie, A.D. Mohite, S.E. Dutton, R.H. Friend, A. Sadhanala, *High Open-Circuit Voltages in Tin-Rich Low-Bandgap Perovskite-Based Planar Heterojunction Photovoltaics*, Adv. Mater. 29 (2017) 1604744. doi:10.1002/adma.201604744.

[27] Z. Yang, A. Rajagopal, C.C. Chueh, S.B. Jo, B. Liu, T. Zhao, A.K.Y. Jen, *Stable Low-Bandgap Pb–Sn Binary Perovskites for Tandem Solar Cells*, Adv. Mater. 28 (2016) 8990–8997. doi:10.1002/adma.201602696.

[28] S.J. Lee, S.S. Shin, Y.C. Kim, D. Kim, T.K. Ahn, J.H. Noh, J. Seo, S. Il Seok, *Fabrication of Efficient Formamidinium Tin Iodide Perovskite Solar Cells through SnF2-Pyrazine Complex*, J. Am. Chem. Soc. 138 (2016) 3974–3977. doi:10.1021/jacs.6b00142.

[29] X. Xu, C.C. Chueh, P. Jing, Z. Yang, X. Shi, T. Zhao, L.Y. Lin, A.K.Y. Jen, *High-Performance Near-IR Photodetector Using Low-Bandgap* $MA_{0.5}FA_{0.5}Pb_{0.5}Sn_{0.5}I_3$ *Perovskite*, Adv. Funct. Mater. 27 (2017) 1–6. doi:10.1002/adfm.201701053.

[30] W. Wang, D. Zhao, F. Zhang, L. Li, M. Du, C. Wang, Y. Yu, Q. Huang, M. Zhang, L. Li, J. Miao, Z. Lou, G. Shen, Y. Fang, Y. Yan, *Highly Sensitive Low-Bandgap Perovskite Photodetectors with Response from Ultraviolet to the Near-Infrared Region*, Adv. Funct. Mater. 27 (2017) 1703953. doi:10.1002/adfm.201703953.

[31] M. Burgelman, P. Nollet, S. Degrave, *Modelling polycrystalline semiconductor solar cells, Thin Solid Films*. 361 (2000) 527–532. doi:10.1016/S0040-6090(99)00825-1.

[32] C. Li, Z. Song, D. Zhao, C. Xiao, B. Subedi, N. Shrestha, M.M. Junda, C. Wang, C. Jiang, M. Al-Jassim, R.J. Ellingson, N.J. Podraza, K. Zhu, Y. Yan, *Reducing Saturation-Current Density to Realize High-Efficiency Low-Bandgap Mixed Tin–Lead Halide Perovskite Solar Cells*, Adv. Energy Mater. 9 (2019) 1803135. doi:10.1002/aenm.201803135.

[33] B. Subedi, C. Li, M.M. Junda, Z. Song, Y. Yan, N.J. Podraza, *Effects of intrinsic and atmospherically induced defects in narrow bandgap* $(FASnI_3)_x(MAPbI_3)_{1-x}$ *perovskite films and solar cells*, J. Chem. Phys. 152 (2020) 064705. doi:10.1063/1.5126867.

[34] W. Abdelaziz, A. Shaker, M. Abouelatta, A. Zekry, *Possible efficiency boosting of non-fullerene acceptor solar cell using device simulation*, Opt. Mater. (Amst). 91 (2019) 239–245. doi:10.1016/j.optmat.2019.03.023.

[35] G. Xu, P. Bi, S. Wang, R. Xue, J. Zhang, H. Chen, W. Chen, X. Hao, Y. Li, Y. Li, *Integrating Ultrathin Bulk-Heterojunction Organic Semiconductor Intermediary for High-Performance Low-Bandgap Perovskite Solar Cells with Low Energy Loss*, Adv. Funct. Mater. 28 (2018) 1–8. doi:10.1002/adfm.201804427.

[36] G. Kapil, T. Bessho, C.H. Ng, K. Hamada, M. Pandey, M.A. Kamarudin, D. Hirotani, T. Kinoshita, T. Minemoto, Q. Shen, T. Toyoda, T.N. Murakami, H. Segawa, S. Hayase, *Strain Relaxation and Light Management in Tin-Lead Perovskite Solar Cells to Achieve High Efficiencies*, ACS Energy Lett. 4 (2019) 1991–1998. doi:10.1021/acsenergylett.9b01237.

[37] G. Kapil, T.S. Ripolles, K. Hamada, Y. Ogomi, T. Bessho, T. Kinoshita, J. Chantana, K. Yoshino, Q. Shen, T. Toyoda, T. Minemoto, T.N. Murakami, H. Segawa, S. Hayase, *Highly Efficient 17.6% Tin-Lead Mixed Perovskite Solar Cells Realized through Spike Structure*, Nano Lett. 18 (2018) 3600–3607. doi:10.1021/acs.nanolett.8b00701.

[38] M. Stolterfoht, P. Caprioglio, C.M. Wolff, J.A. Márquez, J. Nordmann, S. Zhang, D. Rothhardt, U. Hörmann, Y. Amir, A. Redinger, L. Kegelmann, F. Zu, S. Albrecht, N. Koch, T. Kirchartz, M. Saliba, T. Unold, D. Neher, *The impact of energy alignment and interfacial recombination on the internal and external open-circuit voltage of perovskite solar cells*, Energy Environ. Sci. 12 (2019) 2778–2788. doi:10.1039/c9ee02020a.

[39] Y. Raoui, H. Ez-Zahraouy, S. Kazim, S. Ahmad, *Energy level engineering of charge selective contact and halide perovskite by modulating band offset: Mechanistic insights*, J. Energy Chem. 54 (2021) 822–829. doi:10.1016/j.jechem.2020.06.030.

[40] N. Lakhdar, A. Hima, *Electron transport material effect on performance of perovskite solar cells based on* $CH_3NH_3GeI_3$, Opt. Mater. 99 (2020) 109517. doi:10.1016/j.optmat.2019.109517.

[41] Z. Ni, C. Bao, Y. Liu, Q. Jiang, W.Q. Wu, S. Chen, X. Dai, B. Chen, B.

Hartweg, Z. Yu, Z. Holman, J. Huang, *Resolving spatial and energetic distributions of trap states in metal halide perovskite solar cells*, Science. 367 (2020) 1352–1358. doi:10.1126/science.aba0893.

[42] M.S. Chowdhury, S.A. Shahahmadi, P. Chelvanathan, S.K. Tiong, N. Amin, K. Techato, N. Nuthammachot, T. Chowdhury, M. Suklueng, *Effect of deep-level defect density of the absorber layer and n/i interface in perovskite solar cells by SCAPS-1D*, Results Phys. 16 (2020) 102839. doi:10.1016/j.rinp.2019.102839.

[43] T. Jiang, Z. Chen, X. Chen, T. Liu, X. Chen, W.E.I. Sha, H. Zhu, Y. (Michael) Yang, *Realizing High Efficiency over 20% of Low-Bandgap Pb–Sn-Alloyed Perovskite Solar Cells by In Situ Reduction of Sn^{4+}*, Sol. RRL. 4 (2020) 1900467. doi:10.1002/solr.201900467.

[44] K. Frohna, S.D. Stranks, *Hybrid perovskites for device applications, in: Handb. Org. Mater. Electron. Photonic Devices*, Elsevier, 2019: pp. 211–256. doi:10.1016/B978-0-08-102284-9.00007-3.

[45] S.D. Stranks, G.E. Eperon, G. Grancini, C. Menelaou, M.J.P. Alcocer, T. Leijtens, L.M. Herz, A. Petrozza, H.J. Snaith, *Electron-Hole Diffusion Lengths Exceeding 1 Micrometer in an Organometal Trihalide Perovskite Absorber*, Science. 342 (2013) 341–344. doi:10.1126/science.1243982.

[46] T.S. Ripolles, D. Yamasuso, Y. Zhang, M.A. Kamarudin, C. Ding, D. Hirotani, Q. Shen, S. Hayase, *New Tin(II) Fluoride Derivative as a Precursor for Enhancing the Efficiency of Inverted Planar Tin/Lead Perovskite Solar Cells*, J. Phys. Chem. C. 122 (2018) 27284–27291. doi:10.1021/acs.jpcc.8b09609.

[47] C. Li, J. Lu, Y. Zhao, L. Sun, G. Wang, Y. Ma, S. Zhang, J. Zhou, L. Shen, W. Huang, *Highly Sensitive, Fast Response Perovskite Photodetectors Demonstrated in Weak Light Detection Circuit and Visible Light Communication System*, Small. 15 (2019) 1903599. doi:10.1002/smll.201903599.